On-the-Fly Bayesian Active Learning of Interpretable Force Fields for Atomistic Rare Events

Jonathan Vandermause,[1,2] Steven B. Torrisi,[1] Simon Batzner,[2,3] Alexie M. Kolpak,[4] and Boris Kozinsky[2,5]

[1]*Department of Physics, Harvard University, Cambridge, MA 02138, USA*

[2]*John A. Paulson School of Engineering and Applied Sciences, Harvard University, Cambridge, MA 02138, USA*

[3]*Center for Computational Engineering, Massachusetts Institute of Technology, Cambridge, MA 02139, USA*

[4]*Department of Mechanical Engineering, Massachusetts Institute of Technology, Cambridge, MA 02139, USA*

[5]*Bosch Research, Cambridge, MA 02139, USA*

(Dated: April 18, 2022)

Abstract

Machine learning based interatomic potentials currently require manual construction of training sets consisting of thousands of first principles calculations and are often restricted to single-component and nonreactive systems. This severely limits the practical application of these models due to both low training efficiency and limited accuracy in treating important rare events such as reactions and diffusion. We present an adaptive Bayesian inference method for automating and accelerating the on-the-fly construction of accurate interatomic force fields using structures drawn from molecular dynamics simulations. Within an online active learning algorithm, the internal uncertainty of a Gaussian process regression model is used to decide whether to accept the model prediction or to perform a first principles calculation to augment the training set of the model. The method is applied to a range of single- and multi-component systems and shown to achieve state-of-the-art accuracy with minimal *ab initio* data.

I. INTRODUCTION

Recent machine learning (ML) approaches to modeling the Born-Oppenheimer potential energy surface (PES) have been shown to approach first principles accuracy for a number of molecular and solid-state systems [1–10]. These methods provide a promising path toward fast, accurate, and large-scale materials simulations with the accuracy of density functional theory (DFT) and the computational efficiency of classical molecular dynamics (MD). However, most ML potentials return point estimates of the quantities of interest (typically energies, forces, and stresses) rather than a predictive distribution that reflects model uncertainty, making the incorporation of accurate uncertainty estimates into ML models of the PES an outstanding challenge [11–17]. Without model uncertainty, a laborious fitting procedure is required, which usually involves selecting thousands of reference structures from a database of first principles calculations. At test time, lack of predictive uncertainty makes it difficult to determine when the fitted model is trustworthy, leading to unreliable results and lack of guidance on how to update the model in the presence of new data.

Here, we show that active learning based on Gaussian process (GP) regression can accelerate and automate the training of high-quality force fields by making use of accurate internal estimates of model error. By combining DFT with GP regression during molecular dynamics simulations, accurate force fields for a range of single- and multi-element systems are obtained with $\sim$ 100 DFT calls. Moreover, we demonstrate that the model can be flexibly and automatically updated when the system deviates from previous training data. Such a reduction in the computational cost of training and updating potentials promises to extend ML modeling to a much wider class of materials than has been possible to date. The method is shown to successfully model rapid crystal melts and rare diffusive events, and so we call our method FLARE: Fast Learning of Atomistic Rare Events, and make the open-source software freely available online [18].

The key contribution of this work that makes on-the-fly learning possible is the development of a fully interpretable low-dimensional and nonparametric regression model of the PES that provides trustworthy estimates of model uncertainty. Typical ML schemes for modeling the PES involve regression over a high-dimensional descriptor space chosen either on physical grounds [19, 20] or learned directly from *ab initio* data [6, 10]. These approaches require building highly flexible models with many physically non-interpretable parameters,

complicating the task of inferring a posterior distribution over possible models. We instead bypass the need for a high dimensional descriptor by imposing a physical prior that constrains the model to n-body interactions, with high accuracy observed in practice with two- and three-body models. Because the low-dimensional descriptor space of our models can be sampled with a small amount of training data, our method avoids sparsification, a procedure that is used in Gaussian approximation potentials to make inference tractable with many-body descriptors like SOAP [20–22], but that is also known to degrade the quality of GP variance estimates [23]. The learning task is simplified as a result, making it possible to automatically tune the model's hyperparameters in a data-driven fashion and derive trustworthy estimates of model uncertainty. This opens the door to a practical uncertainty-driven scheme for selecting training points "on-the-fly" [24], allowing an accurate potential to be learned with a minimal number of relatively expensive first principles calculations.

The resulting GP-based potentials are interpretable in three important respects. First, the underlying energy model of the GP is a physically motivated sum over n-body contributions, such that each cluster of $n-1$ neighbors in an atom's environment makes a direct contribution to the force on that atom. This establishes a connection to previous, physically motivated interatomic potentials, most notably the Stillinger-Weber potential [25], which also sums over two- and three-body contributions but is limited to a specific analytic form. Our models, by contrast, learn nonparametric two- and three-body functions directly from *ab initio* data, allowing the models to generalize well to complex multi-element systems, as we show in Section III C. Second, the model is descriptor-free, relying on a kernel that directly compares interatomic distances of clusters of atoms. As a result, the only free parameters in the model are a small set of hyperparameters of the GP kernel function, each of which has a direct interpretation and can be rigorously optimized by maximizing the log marginal likelihood of the training data (Section II A). Neural network and Gaussian approximation potentials, on the other hand, rely on complex, high-dimensional descriptors of an atom's environment, making it less apparent how the force acting on an atom is related to the configuration of its neighbors. Finally, and most importantly for online learning, the uncertainty estimates of our GP models break down into two contributions: the predictive variance $\mathcal{V}$, which is determined by distance from the training set and characterizes the epistemic uncertainty associated with a new atomic environment, and the noise variance σ_n^2, which characterizes fundamental variability in the training data that cannot be captured by

the model. The interpretable uncertainties derived from the GP model provide a principled basis for automated training, in which an atomic environment is added to the training set of the model when the predictive variance $\mathcal{V}$ exceeds a chosen multiple of the noise variance, as described in Section II C.

Other on-the-fly learning schemes for force field training have been proposed in the literature, and we discuss them briefly here to place our method in context. Rupp *et al.* [26] and more recently Uteva *et al.* [27] used GP regression to construct potential energy surfaces for small molecular systems with active learning. On-the-fly force field training for extended material systems was first proposed by Li, Kermode, and De Vita [24], but the method relied on performing DFT calculations to evaluate model error due to a lack of correlation between the internal error of their GP model and the true model error [28]. Podryabinkin and Shapeev developed an on-the-fly method for their linear moment tensor potentials [29] using the D-optimality criterion, which provides an internal information-theoretic measure of distance from the training set [12], with subsequent applications to molecules, alloys, and crystal structure prediction [17, 30, 31]. The D-optimality criterion is usually restricted to linear models and does not provide direct error estimates on model predictions. More recently, Jinnouchi *et al.* combined the single-element SOAP kernel with Bayesian linear regression to obtain direct Bayesian error estimates on individual force components, which was used to perform on-the-fly training of force fields to study melting points and perovskite phase transitions [32, 33]. This approach relies on differences between the atomic environments of atoms of distinct species, and may be challenging to apply to multi-element systems in which atoms of distinct species occupy otherwise identical sites in the crystal, as in the nickel titanium example discussed in Section III C. The method presented here possesses four important features that have not been simultaneously achieved before: it is nonparametric, exactly Bayesian, explicitly multi-element, and can be mapped to highly efficient classical potentials, and we therefore expect it to find wide application to a range of complex materials.

The paper is organized as follows. In Section II A, we present fully covariant and explicitly multi-element n-body force kernels for GP regression, building on the work of Glielmo *et al.* [34–36]. In Section II B, the predicted errors of the resulting GP models are shown to provide good agreement with the actual model error. Section II C presents the FLARE algorithm, which makes use of these model errors to automate the training of interatomic potentials.

Section III then applies FLARE to several aluminum simulations, including melting and vacancy/adatom diffusion, and Section III C demonstrates the generality of the method by applying it to carbon, silicon, aluminum oxide, nickel titanium, and two-dimensional boron nitride.

II. METHODOLOGY

A. Gaussian process force fields with covariant n-body kernels

To reason about model uncertainty, we use *ab initio* force data to construct GP models, an established Bayesian approach to describing prior and posterior distributions over unknown functions [23]. As proposed by Glielmo *et al.* [34–36], GP models of the potential energy surface can be systematically decomposed into n-body energy contributions, such that the local energy assigned to atom i in the system takes the form

$$E_i = \sum_{n=2}^{N} \sum_{i_{n-1}>...>i_1 \in \rho_i^{(n)}} \varepsilon_n(\mathbf{s}_{i,i_1,...,i_{n-1}}, \mathbf{d}_{i,i_1,...,i_{n-1}}), \tag{1}$$

where the outer sum ranges over each n-body contribution to the energy up to some maximum order N and the inner sum ranges over all clusters of n atoms inside finite cutoff spheres surrounding atom i, with $\rho_i^{(n)}$ defined as the set of atoms within a chosen cutoff distance $r_{\text{cut}}^{(n)}$ from atom i (see Fig. 1). Below, we will let ρ_i denote the set of cutoff spheres associated with atom i, and refer to it simply as the atomic environment of atom i. The term $\mathbf{s}_{i,i_1,...,i_{n-1}}$ is the vector $(s_i, s_{i_1}, .., s_{i_{n-1}})$ of chemical species of atoms in the cluster, and $\mathbf{d}_{i,i_1,...,i_{n-1}}$ is an ordered vector of interatomic distances between atoms in the cluster. For example, for clusters of two atoms, this vector consists of a single scalar, $\mathbf{d}_{i,i_1} = (r_{i,i_1})$, where r_{i,i_1} is the distance between the central atom i and atom i_1, and for clusters of three atoms, $\mathbf{d}_{i,i_1,i_2} = (r_{i,i_1}, r_{i,i_2}, r_{i_1,i_2})$. Importantly, because each cluster contribution ε_n depends explicitly on the species of the atoms in the cluster, this approach to modeling the potential energy naturally extends to multi-element systems, as we demonstrate in the Results section below.

As in [35, 36], the covariance between n-body energy contributions (ε_n in Eq. (1)) is defined by a kernel function k_n that directly compares interatomic distances in a rotationally

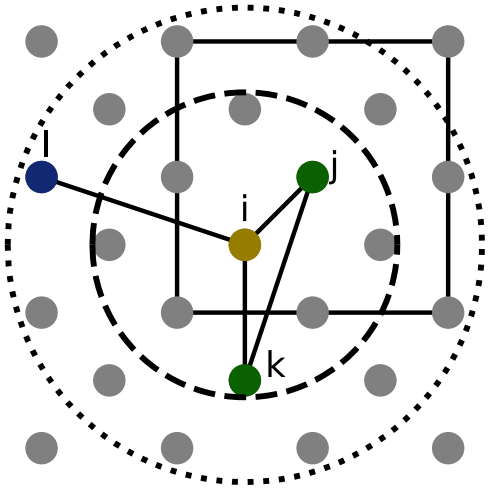

FIG. 1. The two- and three-body cutoffs used in this work. The atomic environment of the central atom (gold) consists of all atoms within the two- and three-body cutoff spheres (dotted and dashed, respectively), including images of atoms in the primary periodic cell (solid square).

invariant fashion, so that the local energy kernel between two atomic environments ρ_i, ρ_j is expressed as a sum over kernels between clusters of atoms:

$$k(\rho_i, \rho_j) = \sum_{n=2}^{N} \sum_{\substack{i_{n-1}>\ldots>i_1\in\rho_i^{(n)} \\ j_{n-1}>\ldots>j_1\in\rho_j^{(n)}}} \sum_{\mathbf{P}_n} \delta_{\mathbf{s}_{i,i_1,\ldots,i_{n-1}},\mathbf{P}_n\mathbf{s}_{j,j_1,\ldots,j_{n-1}}} k_n(\mathbf{d}_{i,i_1,\ldots,i_{n-1}}, \mathbf{P}_n\mathbf{d}_{j,j_1,\ldots,j_{n-1}}). \quad (2)$$

Importantly, this kernel function explicitly distinguishes between distinct species, with the delta function evaluating to 1 if the species vectors of the clusters under comparison are equal and 0 otherwise. The innermost sum of Eq. (2) is over all permutations $\mathbf{P}_n$ of indices of the species and distance vectors of the second cluster, guaranteeing invariance of the model under permutation of atoms of the same species. The resulting force kernel describing the covariance between force components is obtained by differentiating the local energy kernel with respect to the Cartesian coordinates $\vec{r}_{i\alpha}, \vec{r}_{j\beta}$ of the central atoms of ρ_1 and ρ_2,

$$k_{\alpha,\beta}(\rho_i, \rho_j) = \frac{\partial^2 k(\rho_i, \rho_j)}{\partial \vec{r}_{i\alpha} \partial \vec{r}_{j\beta}}, \quad (3)$$

giving an exactly rotationally covariant and energy conserving model of interatomic forces [5, 34, 35]. For completeness, we provide in Appendix B a table of formulae involved in

computing the three-body derivative kernel described by Eq. (3), along with its derivatives with respect to the hyperparameters of the kernel. In this work, we choose $N = 3$, restricting the sum to two- and three-body contributions, as we have found the resulting GP models to be sufficiently expressive to describe with high accuracy a range of single- and multi-element systems while remaining computationally efficient. This is consistent with the findings of Ref. [35], which compared the performance of two-, three-, and many-body kernels and found that many-body models required substantially more training data while only modestly improving performance for several crystals, nanoclusters, and amorphous systems. Further investigation of model accuracy as a function of the maximum order N of the kernel for different types of materials is an interesting area for future study, as it may provide a systematic data-driven approach to characterizing many-body interactions in complex material systems.

For the pair and triplet kernels k_2 and k_3, we choose the squared exponential kernel multiplied by a smooth quadratic cutoff function that ensures the potential is continuous as atoms enter and exit the cutoff sphere,

$$\begin{aligned} k_2(r_{i,i_1}, r_{j,j_1}) &= \sigma_{s,2}^2 \exp\left(-\frac{(r_{i,i_1} - r_{j,j_1})^2}{2\ell_{(2,3)}^2}\right) f_{\text{cut}}(r_{i,i_1}, r_{j,j_1}), \\ k_3(\mathbf{d}_{i,i_1,i_2}, \mathbf{d}_{j,j_1,j_2}) &= \sigma_{s,3}^2 \exp\left(-\frac{||\mathbf{d}_{i,i_1,i_2} - \mathbf{d}_{j,j_1,j_2}||^2}{2\ell_{(2,3)}^2}\right) f_{\text{cut}}(\mathbf{d}_{i,i_1,i_2}, \mathbf{d}_{j,j_1,j_2}), \end{aligned} \tag{4}$$

where $\sigma_{s,(2,3)}$ is the signal variance related to the maximum uncertainty of points far from the training set, $\ell_{(2,3)}$ is the length scale of the two- and three-body contributions, and $||.||$ denotes the vector 2-norm. The force $\vec{f_i}$ on each atom i and its corresponding predictive variance $\mathcal{V}[\vec{f_i}]$ are computed using the standard GP relations [23],

$$\begin{aligned} f_{i\alpha} &= \bar{k}_{i\alpha}^T \left(K + \sigma_n^2 I\right)^{-1} \bar{y} \\ \mathcal{V}[f_{i\alpha}] &= k_{\alpha,\alpha}(\rho_i, \rho_i) - \bar{k}_{i\alpha}^T \left(K + \sigma_n^2 I\right)^{-1} \bar{k}_{i\alpha}, \end{aligned} \tag{5}$$

where $\bar{k}_{i\alpha}$ is the vector of force kernels between ρ_i and the atomic environments in the training set, i.e. $\bar{k}_{i\alpha,j\beta} = k_{\alpha,\beta}(\rho_i, \rho_j)$, K is the covariance matrix $K_{m\alpha,n\beta} = k_{\alpha,\beta}(\rho_m, \rho_n)$ of the training points, $\bar{y}$ is the vector of forces acting on the atoms in the training set, and σ_n is a hyperparameter that characterizes observation noise. In all models in this work, the hyperparameters $\sigma_2, \sigma_3, \ell_2, \ell_3$, and σ_n are optimized with SciPy's implementation of the

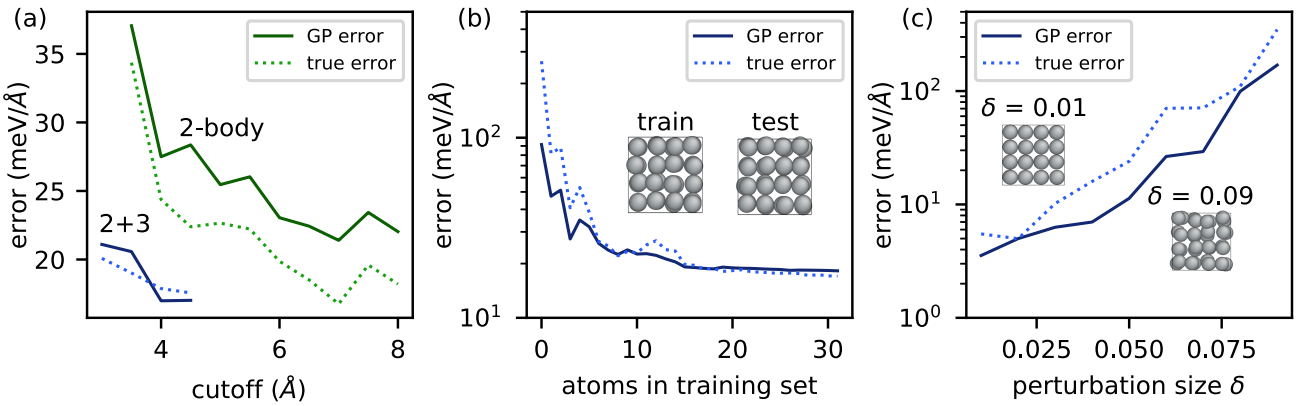

FIG. 2. Correlation of optimized Gaussian process noise σ_n and predictive variance $\mathcal{V}$ with the root mean square error on independent test structures. (a) The optimized noise parameter σ_n (solid) and root mean squared error (dotted) as a function of the cutoff radius r_{cut} of the atomic environment. (b) Combined model error $\sqrt{\sigma_n^2 + \sigma_{\text{mean}}^2}$ as a function of the number of training atoms. (c) Mean predictive standard deviation σ_{mean} (solid) and RMSE (dotted) on test structures with atomic coordinates perturbed from $\delta = 1\%$ to 9% of the lattice parameter.

BFGS algorithm [37] by maximizing the log marginal likelihood of the training data, which has an exact analytic form [23]. Computation of the log marginal likelihood involves inverting the covariance matrix K and is efficient if the model is trained on fewer than ~ 1000 points. This data-driven approach to selecting model hyperparameters stands in contrast to other GP models of the PES, in which hyperparameters are chosen heuristically [4].

B. Characterization of model uncertainty

To justify an on-the-fly learning algorithm, we first characterize the uncertainty and noise estimates of GP models constructed with the two- and three-body kernels described above, and compare them against test errors on out-of-sample structures. Remarkably, the optimized noise parameter σ_n and predictive variance $\mathcal{V}$ defined in Eq. (5) are found to provide a sensitive probe of true model error, with σ_n capturing the baseline error level of model predictions on atomic environments that are well represented in the training set and $\mathcal{V}$ capturing error due to deviation from the training data. We test the relationship between GP error and true error by performing a set of plane-wave DFT calculations on a

32-atom supercell of FCC aluminum with atomic positions randomly perturbed from their equilibrium sites. In Fig. 2(a), all atomic coordinates are randomly perturbed by up to 5% of the lattice parameter, which was set to the experimental value of 4.046 Å. Two- and two-plus-three body GP models are trained on all forces acting on atoms in a single structure and tested on an independently generated structure, with the cutoff radius swept from 3.5 to 8 Å in increments of 0.5 Å (see the inset of Fig. 2(b) for a visual of the training and test structures). For the two-body models, the three-body contribution in Eq. (2) was discarded and only the two-body term was kept. For the two-plus-three body models (lower left of Fig. 2(a)), the 2-body cutoff was held fixed at 6 Å and the 3-body cutoff was swept from 3 to 4.5 Å. The optimized noise parameter σ_n plotted in Fig. 2(a) closely tracks the root mean squared error (RMSE) on the test structure for the range of examined cutoff values. This provides a principled way of selecting the cutoff radius of the GP model, showing that the expected error of the model at a given cutoff can be directly estimated from the optimized noise hyperparameter σ_n when the GP model has been trained on sufficient data.

When the GP model is trained on insufficient data, the predictive standard deviation σ, defined as the square root of the predictive variance $\mathcal{V}$, rises above the baseline noise level σ_n of the model, indicating that the model requires additional training data to make accurate force estimates. The utility of the predictive variance is illustrated in Fig. 2(b). Using the same training and test structures as Fig. 2(a), a GP model is constructed by adding forces on specific atoms to the training set and evaluating the RMSE and GP error after each atomic environment is added. The average GP error $\sqrt{\sigma_n^2 + \sigma_{\text{mean}}^2}$ closely tracks the RMSE, where σ_{mean} is the mean predictive standard deviation over all force components in the test set.

We also demonstrate in Fig. 2(c) that the GP variance provides an accurate indicator of model error when the model is forced to extrapolate on atomic environments that are significantly different from atomic environments in the training set. To show this, a model was trained on a single aluminum structure with atomic coordinates perturbed by $\delta = 5\%$ of the lattice parameter and tested on structures generated with values of δ ranging from 1 to 9%. The mean predictive standard deviation σ_{mean} correlates with the true error across all values of δ, demonstrating the ability of the GP to detect when it is predicting on structures that are far from the training set. This capability is crucial for on-the-fly learning, as the model must be able to flag when additional training data is needed in order to accurately

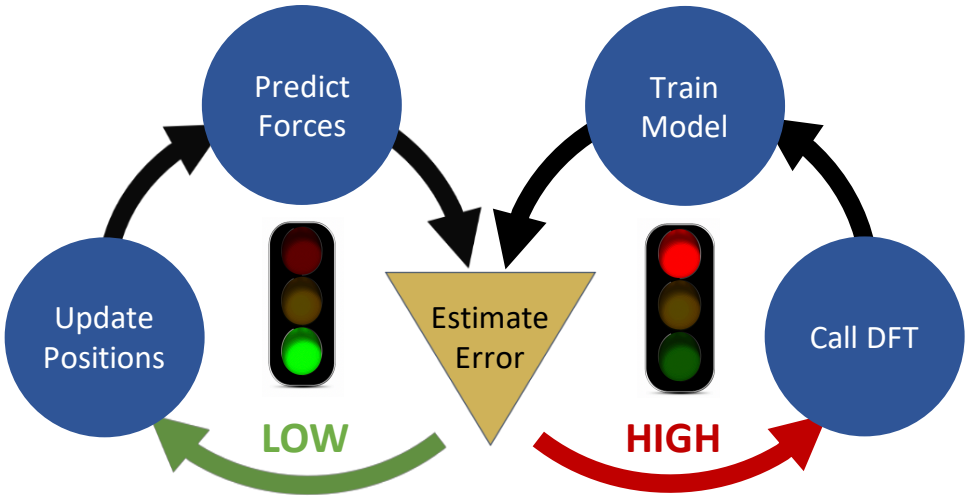

FIG. 3. Fast learning of atomistic rare events (FLARE): an on-the-fly learning algorithm for automatically constructing interatomic potentials. Left loop: Molecular dynamics steps are proposed by the current GP model of the potential energy surface, with the predictive error of the GP monitored at each step. Right loop: If the predictive standard deviation on a force component rises above a chosen multiple of the optimized noise parameter σ_n of the GP, DFT is called and the training set of the GP is updated with the highest uncertainty atomic environments.

estimate forces.

C. FLARE: An on-the-fly learning algorithm

The reliability of the internal GP error estimate is the unique feature of our approach that enables us to implement FLARE, a fully adaptive active learning molecular dynamics method, in which DFT is called only when the predictive standard deviation of the GP model rises above an adaptive threshold σ_{thresh} based on the optimized noise parameter σ_n. As sketched in Fig. 3, the algorithm takes an arbitrary structure as input and begins with a call to DFT, which is used to initialize a GP model. MD steps are then proposed by the GP, with calls to DFT made whenever the predictive standard deviation of a force prediction rises above a chosen multiple of the current noise parameter σ_n of the model, in which case the training set is augmented with the highest uncertainty atomic environments, the precise number $\mathcal{N}_{\text{added}}$ of which can be tuned to increase training efficiency. All hyperparameters, including the noise parameter σ_n, are optimized whenever an atomic environment and its

force components are added to the training set, allowing the error threshold to adapt to novel environments encountered during the simulation. The method is implemented with the FLARE package [18], which couples the Quantum ESPRESSO DFT code [38] to Python-based MD and GP code. Calculations of the kernel and interatomic distances are accelerated with the open-source just-in-time compiler Numba to enable training simulations spanning hundreds of picoseconds [39].

III. RESULTS

A. Aluminum crystal melt

As a first demonstration of the method, we consider a 32-atom bulk aluminum system initialized in the FCC phase at low temperature, with $\mathcal{N}_{\text{added}} = 1$ atomic environment added to the training set whenever the predictive standard deviation exceeds the current noise parameter, $\sigma_{\text{thresh}} = \sigma_n$. As shown in Fig. 4(a), DFT is called often at the beginning of the simulation as the GP model learns a force field suitable for FCC aluminum. After about 30 time steps, the model needs far fewer training points, requiring fewer than 50 DFT calls in the first 5 ps of the simulation. To test the model's ability to actively learn and adapt to changing conditions, the crystal is melted at time $t = 5$ ps by rescaling the velocities of the atoms to give the system an instantaneous temperature of 10^4 K (well above the experimental melting point of aluminum due to the strong finite size effects of the 2x2x2 supercell). The subsequent temperature in the remaining 5 ps of the simulation stabilizes around 5000 K with a radial distribution function consistent with the liquid phase (Fig. 4(c)). As shown in Fig. 4(b), which plots the cumulative number of DFT calls made during the training run, the GP model requires a large number of DFT calls immediately after the crystal melts, as the atomic environments in the liquid phase of aluminum are significantly different from the previous solid-state training data. The noise parameter σ_n of the model (shown in red in Fig. 4(c)) sharply increases as the system enters the liquid phase, reflecting the fact that it is more difficult to model, involving more diverse atomic environments and significantly larger force fluctuations. Because the error threshold σ_{thresh} is set equal to the optimized noise parameter σ_n, the threshold in the liquid phase is higher, and as a result the GP model requires a roughly similar number of DFT calls to learn the solid and

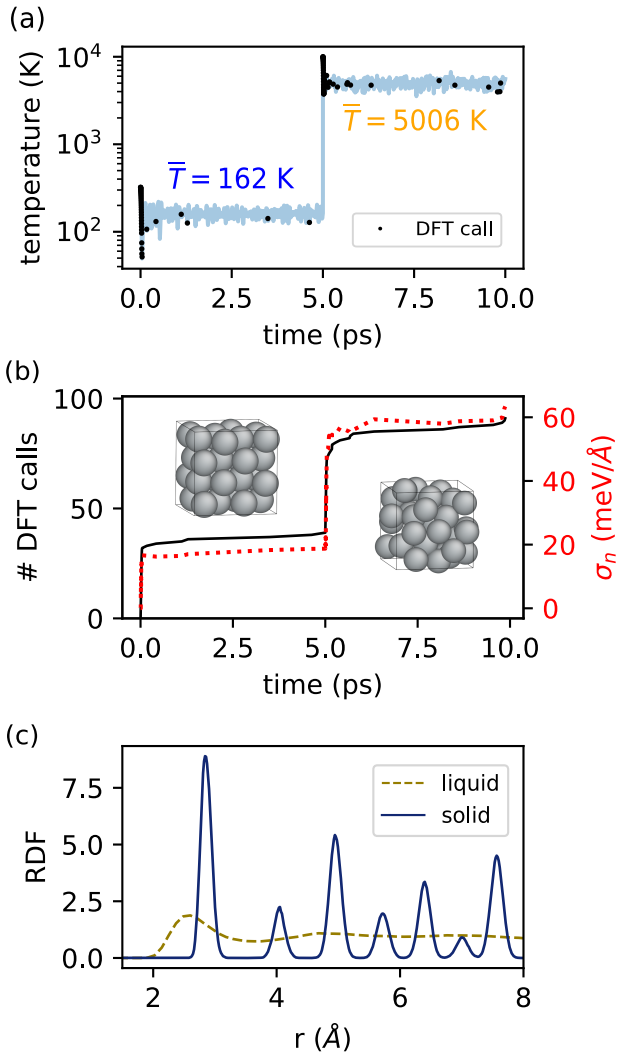

FIG. 4. Active learning of a multi-phase aluminum force field. (a) Instantaneous temperature during a 10 ps on-the-fly MD trajectory generated with the FLARE learning algorithm. The simulation begins in the FCC phase at low temperature and is melted at $t = 5$ ps. When the predicted error on a force component rises above the current noise parameter σ_n of the model, DFT is called (black dots). (b) The number of DFT calls (solid) and optimized noise parameter (dotted) throughout the simulation. A sharp increase is observed when the crystal is melted, illustrating the model's ability to actively learn the liquid phase. (c) During the first 5 ps of the simulation, the radial distribution function (RDF) is consistent with that of an fcc crystal (solid line), while in the final half of the simulation, the system exhibits an RDF characteristic of the liquid phase (dashed).

Test Set	EAM [40]	AGNI [11]	FLARE
FCC Solid	46.1	41.2	**32.9**
Liquid	157.0	128.0	**90.2**

TABLE I. Comparison of the FLARE model of Fig. 4 against other recent classical and machine-learned aluminum potentials. Test structures were drawn from *ab initio* molecular dynamics trajectories of a 2x2x2 supercell of bulk aluminum in the solid and liquid phases. Errors are reported in meV/Å, with lowest errors highlighted in bold.

liquid phases. Fewer than 100 calls are needed in total during the 10 ps of dynamics, with the majority of DFT calls made at the beginning of the simulation and immediately after melting.

The obtained potential is validated by testing the model on two independent 10 ps *ab initio* molecular dynamics (AIMD) simulations of the solid and liquid phases of aluminum. 100 structures were sampled from the AIMD trajectories with 0.1 ps spacing between structures. Force predictions on all test structures were obtained with the GP potential of Fig. 4 and compared against the corresponding DFT values, with the mean absolute error in meV/Å recorded in Table I. For reference, the models are compared against state-of-the-art EAM and ML potentials [11, 40]. Each potential is tested on the same structures, with the FLARE potential reaching the lowest force errors for both trajectories. This is partly due to the fact that the FLARE method optimizes the force field specifically for the simulation of interest, only augmenting the training set when necessary. This bypasses the need to anticipate all possible phases which a system might explore while constructing a potential.

B. Bulk vacancy and surface adatom diffusion

We next demonstrate that FLARE can be used to train force fields that dramatically accelerate simulations of rare-event dynamics over timescales spanning hundreds of picoseconds by applying the method to aluminum bulk vacancy diffusion and surface adatom diffusion. For bulk vacancy training, a 1 ns simulation was initialized by removing one atom from an equilibrium 32-atom FCC structure and setting the instantaneous initial temperature to 1500 K, giving a mean temperature of 734 K across the simulation. The GP model was

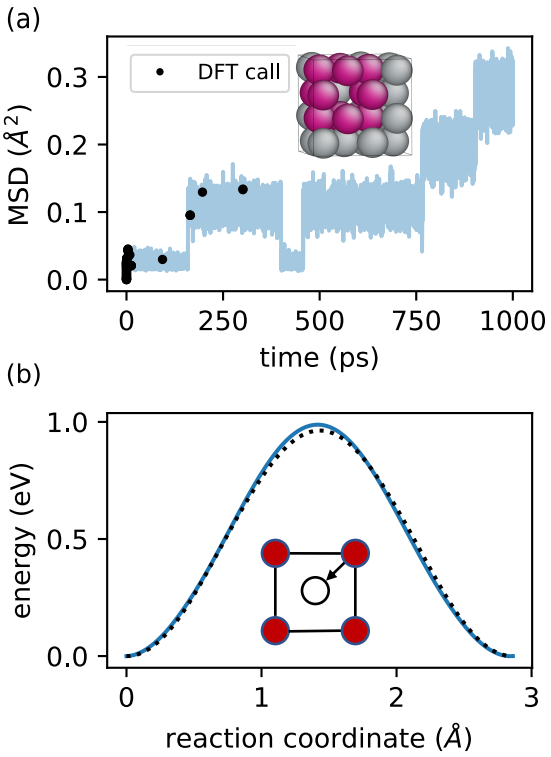

FIG. 5. On-the-fly force field learning of vacancy diffusion in bulk aluminum. (a) Mean squared displacement during a FLARE training run of duration 1 ns. The majority of DFT calls occur at the beginning of the run, with no additional calls required after the first 400 ps. Inset: Bulk fcc aluminum with a vacancy, with atoms closest to the vacancy highlighted. (b) Barrier predicted by the resulting potential for vacancy migration along a high symmetry transition path, in close agreement with the *ab initio* barrier.

constructed with a two-body kernel with cutoff $r_{\text{cut}}^{(2)} = 5.4$ Å, giving a final optimized noise parameter of $\sigma_n = 70.2$ meV/Å. Discarding the three-body contribution significantly accelerates the simulation while still achieving low force errors due to the simplicity of the single-defect bulk crystalline phase, opening up nanosecond timescales. As shown in Fig. 5(a), most DFT calls are made early on in the simulation, and after the first ~ 400 ps, no additional DFT calls are required. The model predicts vacancy hops every few hundred picoseconds, which appear as sharp jumps in the mean squared displacement plotted in Fig. 5(a). To check the accuracy of the underlying energy model of the GP, DFT energies were computed along the high symmetry transition path sketched in the inset of Fig. 5(b), with a nearest neighbor migrating into the vacancy while all other atoms in the simulation cell

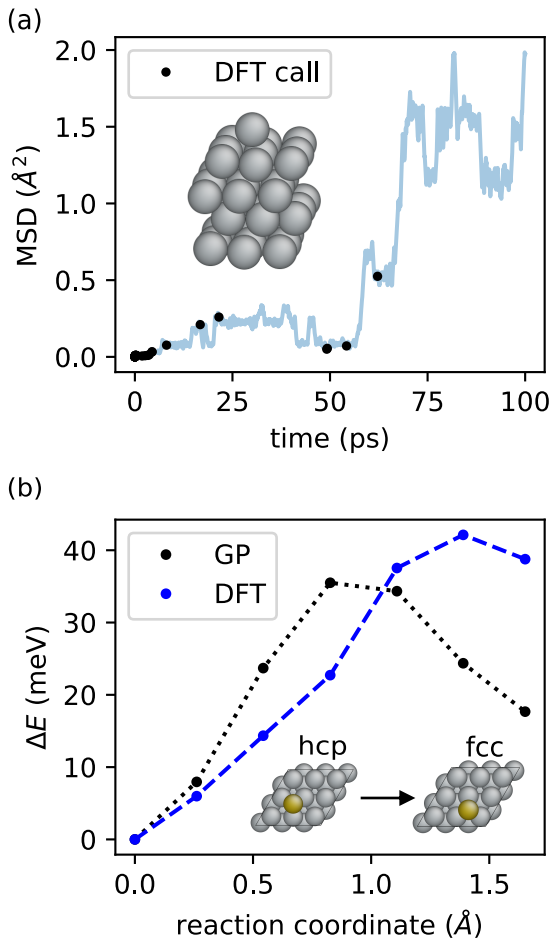

FIG. 6. On-the-fly force field learning of adatom diffusion on a (111) aluminum surface. (a): Mean squared displacement during a FLARE training run of duration 100 ps, with sharp jumps in the MSD signalling movement of the adatom on the Al surface. An example structure drawn from the training simulation is shown in the inset. (b) Nudged elastic band energies of the hcp-to-fcc transition computed with the trained GP potential (black). Energy differences are relative energy of the first NEB image. DFT energies are computed for each image (blue), confirming the adatom's energetic preference for the hcp site.

are kept frozen at their fcc lattice sites. The GP force predictions along the transition path were integrated to give an estimate of the energy barrier, showing close agreement with the *ab initio* DFT values. The entire FLARE training run, including DFT calculations, GP hyperparameter optimization, force evaluations and MD updates, were performed on a 32-core machine in 68.8 hours of wall time. Individual DFT calls required over a minute of wall

time on average, making FLARE over 300 times faster than an equivalent AIMD run.

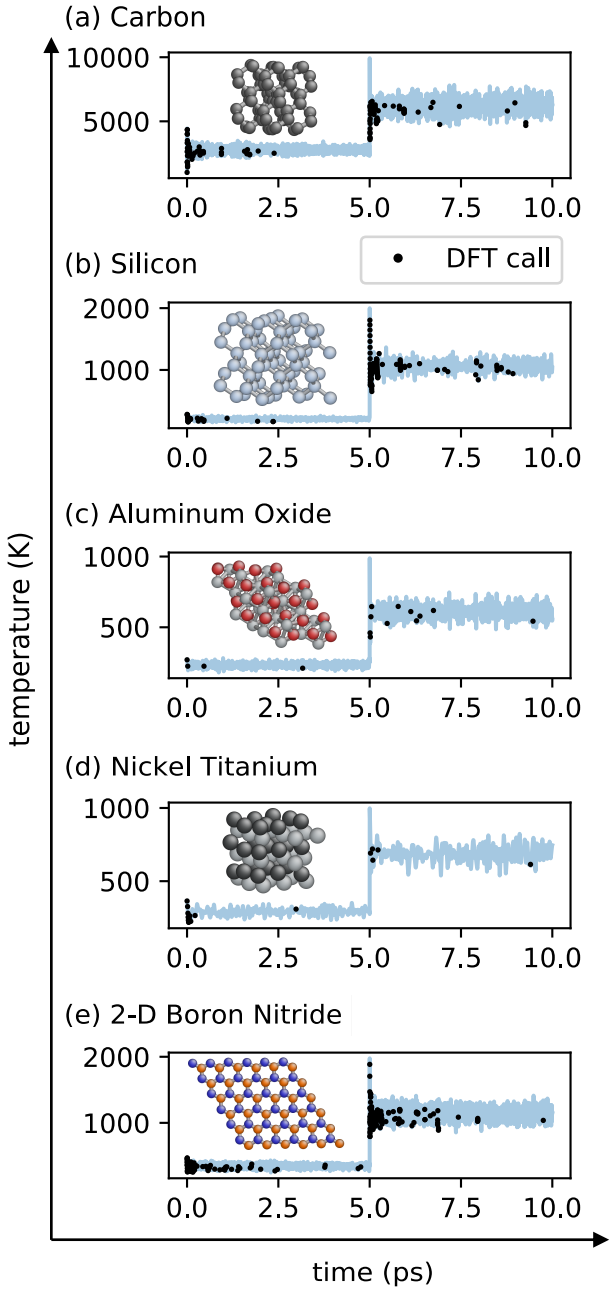

FIG. 7. On-the-fly force field learning applied to a range of single- and multi-component systems. In each training run, the instantaneous temperature (blue) was increased at time $t = 5.0$ ps, triggering DFT calls and updates to the GP model (black dots) caused by model detection of novel atomic environments. Example structures from each simulation are shown in the insets.

To test the accuracy of FLARE on a subtler transition with a significantly lower energy barrier, we consider aluminum adatom diffusion on a four-layer (111) aluminum slab, with

a representative structure shown in the inset of Fig. 5(a). For this system, three-body contributions were found to considerably increase the accuracy of the potential, with a 7 Å two-body cutoff and 4.5 Å three-body cutoff giving an optimized noise parameter of $\sigma_n = 44.2$ meV/Å after the final DFT call at $t = 62.2$ ps (Fig. 6(a)). The energy barrier for adatom diffusion from the hcp to fcc site (illustrated in the inset of Fig. 6(b)) is more than an order of magnitude smaller than vacancy migration in the bulk, providing a stringent test of the GP potential to describe slight energy differences on the solid state surface. To validate the energetics of the potential, a 7-image nudged elastic band (NEB) calculation characterizing the transition from the hcp to fcc adatom sites was performed using the Atomic Simulation Environment [41] with the GP energy predictions shown in black in Fig. 6(b). The DFT energies of each image of the NEB calculation are shown in blue (relative to the energy of the first image), showing agreement to within ≈ 20 meV for each image and confirming the GP's prediction of a slight energetic preference for the hcp site in equilibrium.

C. General applicability

Finally, we demonstrate that FLARE can be widely applied to diverse systems, including covalently bonded insulators and semiconductors, as well as oxides, alloys, and two-dimensional materials. In Fig. 7, FLARE training runs are performed for five representative systems — carbon, silicon, aluminum oxide, nickel titanium, and two-dimensional boron nitride — with the instantaneous temperature of each system rescaled at $t = 5$ ps to illustrate the model's ability to detect and adapt to novel atomic environments. Training details, including the total number of atoms in the training simulation $\mathcal{N}_{\text{atoms}}$, the two- and three-body cutoffs $r_{(2,3)}$, the error threshold for updating the GP σ_{thresh}, the number of atoms added at each update $\mathcal{N}_{\text{added}}$, the total number of DFT calls made $\mathcal{N}_{\text{DFT}}$, and the total wall time for training t_{wall}, are recorded in the left half of Table II. To accelerate training of the nickel titanium potential, which required expensive self-consistent field calculations, the error threshold was set to twice the noise parameter, $\sigma_{\text{thresh}} = 2\sigma_n$, significantly reducing the total number of DFT calls needed to ~ 20 (as shown in Fig. 7(d) and Table II). Adding multiple atoms to the training set at each DFT call also had the effect of reducing the total number of DFT calls needed, as apparent in the aluminum oxide training run, for which $\mathcal{N}_{\text{added}} = 30$ and only 16 DFT calls were needed in total to train the model. Each training

	Training							Validation			
	$\mathcal{N}_{\text{atoms}}$	r_2 (Å)	r_3 (Å)	σ_{thresh}	$\mathcal{N}_{\text{added}}$	$\mathcal{N}_{\text{DFT}}$	t_{wall} (hours)	T (K)	MSE (eV/Å)	P_{95} (eV/Å)	Ratio
C	64	4.0	2.75	σ_n	1	107	11.3	3710	0.42	7.45	0.056
Si	64	6.0	4.2	σ_n	5	133	64.4	620	0.077	1.54	0.050
Al_2O_3	80	4.5	3.5	σ_n	30	16	20.6	533	0.14	1.85	0.076
NiTi	54	4.48	3.2	$2\sigma_n$	10	18	33.3	510	0.10	1.00	0.104
BN	72	5.1	4.0	σ_n	1	237	31.4	677	0.092	3.24	0.029

TABLE II. Training and validation details of the FLARE potentials shown in Fig. 7.

run was performed on a 32-core machine and took between 11.3 and 64.4 hours of wall time (for silicon and carbon, respectively). We emphasize that the training procedure for each material is fully automatic, with the training set and hyperparameters updated on-the-fly without any human guidance.

To validate the potentials, independent NVE molecular dynamics trajectories of duration 10 ps were generated with each model, with DFT calculations performed for 10 MD frames spaced equally across the simulation and compared against the corresponding GP predictions. We find low mean squared errors (MSE) of around 0.1 eV/Å for four of the five systems, and for C find a MSE of 0.42 eV/Å. The MSE over all force component predictions in the 10 representative frames is reported in Table II for each validation run. In order to illustrate the range of force magnitudes present in the simulation, we also report the 95th percentile of the absolute force components in these frames, with the ratio of the two reported in the final column of Table II. The resulting ratios lie between 3% and 10%, similar to the same ratios reported in a recent study of amorphous carbon with a Gaussian approximation potential [4]. The mean temperature $\overline{T}$ of each MD run (reported in the right side of Table II) was chosen to lie within the range of temperatures present in the training simulations of Fig. 7.

IV. CONCLUSION

In summary, we have presented a method for rapidly and automatically training Gaussian process models that provide highly accurate force estimates and reliable internal estimates

of model uncertainty. The model's noise hyperparameter and predictive variance are shown to correlate well with the true out-of-sample error, providing an interpretable, principled basis for active learning of a force field model during molecular dynamics. The FLARE nonparametric interatomic potential model described here requires a much smaller number of atomic environments to converge the model than other state-of-the-art machine learning approaches, and is therefore well-suited to settings where large databases of *ab initio* data are too expensive to compute. Our models have a simple, accurate, and physically interpretable underlying energy model, which can be used to map the potential to a faster regression model approaching the efficiency of a classical force field [35]. This provides a path toward potentials tailored to individual applications with the accuracy of DFT at several orders of magnitude lower computational cost, which we expect to considerably expand the range of materials that can be accurately studied with atomistic simulation. Particularly promising is the application of the FLARE engine to dynamical systems dominated by rare diffusion or reaction events, that are very difficult to treat with existing *ab initio*, classical force field, or machine learning models.

V. ACKNOWLEDGEMENTS

We thank Yu Xie, Lixin Sun, and Aldo Glielmo for helpful discussions. B.K. and J.V. acknowledge funding support from Bosch Research. A.M.K. and S.B. acknowledge funding from the MIT-Skoltech Center for Electrochemical Energy Storage. S.B.T. is supported by the Department of Energy Computational Science Graduate Fellowship under grant DE-FG02-97ER25308.

VI. COMPETING INTERESTS

The authors declare no competing financial or non-financial interests.

VII. DATA AVAILABILITY

The trained Gaussian process models and other simulation data are available from the authors upon request.

VIII. AUTHOR CONTRIBUTIONS

J.V. conceived the study and is the primary developer of the FLARE code. S.B.T. and S.B. assisted with code development. B.K. supervised the work and contributed to algorithm development. All authors participated in discussions and helped write the manuscript.

Material	Pseudopotential	K-points	Energy (Ry)	Density (Ry)
Al (Fig. 2)	Al.pbe-n-kjpaw-psl.1.0.0.UPF	7x7x7	29	143
Al (Figs. 4-5)	Al.pbe-n-kjpaw-psl.1.0.0.UPF	2x2x2	29	143
Al (Fig. 6)	Al.pbe-n-kjpaw-psl.1.0.0.UPF	4x4x2	29	143
C	C.pbe-n-kjpaw_psl.1.0.0.UPF	2x2x2	40	326
Si	Si.pbe-n-kjpaw_psl.1.0.0.UPF	Γ	44	175
Al_2O_3	Al.pbe-n-kjpaw-psl.1.0.0.UPF O.pbe-n-kjpaw_psl.1.0.0.UPF	Γ	47	323
NiTi	Ni.pz-n-rrkjus_psl.0.1.UPF Ti.pz-spn-rrkjus_psl.1.0.0.UPF	2x2x2	52	576
BN	B.pbe-n-kjpaw_psl.1.0.0.UPF N.pbe-n-kjpaw_psl.1.0.0.UPF	Γ	44	325

TABLE III. Details of DFT calculations performed in this work. All pseudopotentials are available in the Quantum Espresso pseudopotential library [43, 44].

Appendix A: Computational details

All DFT calculations were performed using Quantum Espresso 6.2.1, with pseudopotentials, k-point meshes, plane-wave energy cutoffs, and charge density energy cutoffs for all calculations reported in Table III. All molecular dynamics trajectories, including AIMD runs, were performed in the NVE ensemble using the Verlet algorithm. Atomistic visualizations were created using Atomeye [42].

Appendix B: Derivative kernel expressions

Expressions used to compute the three-body force kernel defined in Eq. (2) of the main text are reported in Table IV.

[1] W. J. Szlachta, A. P. Bartók, and G. Csányi, Physical Review B **90**, 104108 (2014).

Energy Kernel	$k_3(\mathbf{d}_{i,i_1,i_2}, \mathbf{d}_{j,j_1,j_2})$	$\sigma_{s,3}^2 k_{\mathrm{SE}}(\mathbf{d}_{i,i_1,i_2}, \mathbf{d}_{j,j_1,j_2}) f_{\mathrm{cut}}(\mathbf{d}_{i,i_1,i_2}) f_{\mathrm{cut}}(\mathbf{d}_{j,j_1,j_2})$
-	$k_{\mathrm{SE}}(\mathbf{d}_{i,i_1,i_2}, \mathbf{d}_{j,j_1,j_2})$	$\exp\left(-\frac{\|\mathbf{d}_{i,i_1,i_2}-\mathbf{d}_{j,j_1,j_2}\|^2}{2\ell^2}\right)$
-	$\mathbf{d}_{j,j_1,j_2}$	$(r_{i,i_1}, r_{i,i_2}, r_{i_1,i_2})$
-	$f_{\mathrm{cut}}(\mathbf{d}_{i,i_1,i_2})$	$f(r_{i,i_1}) f(r_{i,i_2}) f(r_{i_1,i_2})$
-	$f(r)$	$(r - r_{\mathrm{cut}})^2$
Force Kernel	$\frac{\partial^2 k_3}{\partial \vec{r}_{i\alpha} \partial \vec{r}_{j\beta}}$	$\sigma_{s,3}^2(k_0 + k_1 + k_2 + k_3)$
-	k_0	$k_{\mathrm{SE}} \frac{\partial f_{\mathrm{cut}}(\mathbf{d}_{i,i_1,i_2})}{\partial \vec{r}_{i\alpha}} \frac{\partial f_{\mathrm{cut}}(\mathbf{d}_{j,j_1,j_2})}{\partial \vec{r}_{j\beta}}$
-	k_1	$\frac{\partial k_{\mathrm{SE}}}{\partial \vec{r}_{i\alpha}} f_{\mathrm{cut}}(\mathbf{d}_{i,i_1,i_2}) \frac{\partial f_{\mathrm{cut}}(\mathbf{d}_{j,j_1,j_2})}{\partial \vec{r}_{j\beta}}$
-	k_2	$\frac{\partial k_{\mathrm{SE}}}{\partial \vec{r}_{j\beta}} \frac{\partial f_{\mathrm{cut}}(\mathbf{d}_{i,i_1,i_2})}{\partial \vec{r}_{i\alpha}} f_{\mathrm{cut}}(\mathbf{d}_{j,j_1,j_2})$
-	k_3	$\frac{\partial^2 k_{\mathrm{SE}}}{\partial \vec{r}_{i\alpha} \partial \vec{r}_{j\beta}} f_{\mathrm{cut}}(\mathbf{d}_{i,i_1,i_2}) f_{\mathrm{cut}}(\mathbf{d}_{j,j_1,j_2})$
-	$\frac{\partial k_{\mathrm{SE}}}{\partial \vec{r}_{i\alpha}}$	$\frac{k_{\mathrm{SE}} B_1}{\ell^2}$
	B_1	$\frac{(r_{i,i_1}-r_{j,j_1})(\vec{r}_{i_1\alpha}-\vec{r}_{i\alpha})}{r_{i,i_1}} + \frac{(r_{i,i_2}-r_{j,j_2})(\vec{r}_{i_2\alpha}-\vec{r}_{i\alpha})}{r_{i,i_2}}$
-	$\frac{\partial k_{\mathrm{SE}}}{\partial \vec{r}_{j\beta}}$	$-\frac{k_{\mathrm{SE}} B_2}{\ell^2}$
-	B_2	$\frac{(r_{i,i_1}-r_{j,j_1})(\vec{r}_{j_1\beta}-\vec{r}_{j\beta})}{r_{j,j_1}} + \frac{(r_{i,i_2}-r_{j,j_2})(\vec{r}_{j_2\beta}-\vec{r}_{j\beta})}{r_{j,j_2}}$
-	$\frac{\partial^2 k_{\mathrm{SE}}}{\partial \vec{r}_{i\alpha} \vec{r}_{j\beta}}$	$\frac{k_{\mathrm{SE}}}{\ell^4}\left(A\ell^2 - B_1 B_2\right)$
-	A	$\frac{(\vec{r}_{i_1\alpha}-\vec{r}_{i\alpha})(\vec{r}_{j_1\beta}-\vec{r}_{j\beta})}{r_{i,i_1} r_{j,j_1}} + \frac{(\vec{r}_{i_2\alpha}-\vec{r}_{i\alpha})(\vec{r}_{j_2\beta}-\vec{r}_{j\beta})}{r_{i,i_2} r_{j,j_2}}$
ℓ Derivative	$\frac{\partial^3 k_3}{\partial \ell \partial \vec{r}_{i\alpha} \partial \vec{r}_{j\beta}}$	$\sigma_{s,3}^2\left(\frac{\partial k_0}{\partial \ell} + \frac{\partial k_1}{\partial \ell} + \frac{\partial k_2}{\partial \ell} + \frac{\partial k_3}{\partial \ell}\right)$
-	$\frac{\partial k_{\mathrm{SE}}}{\partial \ell}$	$\frac{k_{\mathrm{SE}} \|\mathbf{d}_{i,i_1,i_2}-\mathbf{d}_{j,j_1,j_2}\|^2}{l^3}$
-	$\frac{\partial^2 k_{\mathrm{SE}}}{\partial \ell \partial \vec{r}_{i\alpha}}$	$B_1\left(\frac{1}{\ell^2}\frac{\partial k_{\mathrm{SE}}}{\partial \ell} - \frac{2k_{\mathrm{SE}}}{\ell^3}\right)$
-	$\frac{\partial^2 k_{\mathrm{SE}}}{\partial \ell \partial \vec{r}_{j\beta}}$	$-B_2\left(\frac{1}{\ell^2}\frac{\partial k_{\mathrm{SE}}}{\partial \ell} - \frac{2k_{\mathrm{SE}}}{\ell^3}\right)$
-	$\frac{\partial^3 k_{\mathrm{SE}}}{\partial \ell \partial \vec{r}_{i\alpha} \partial \vec{r}_{j\beta}}$	$\left(A\ell^2 - B_1 B_2\right)\left(\frac{\partial k_{\mathrm{SE}}}{\partial \ell}\frac{1}{\ell^4} - \frac{4k_{\mathrm{SE}}}{\ell^5}\right) + \frac{2k_{\mathrm{SE}} A}{\ell^3}$
σ Derivative	$\frac{\partial^3 k_3}{\partial \sigma_{s,3} \partial \vec{r}_{i\alpha} \partial \vec{r}_{j\beta}}$	$2\sigma_{s,3}(k_0 + k_1 + k_2 + k_3)$

TABLE IV. Quantities used to calculate the three-body force kernel and its derivatives with respect to the hyperparameters ℓ and σ, which are required in the calculation of the log marginal likelihood. Terms in the second column are defined in the third column.

[2] J. Behler, Physical Chemistry Chemical Physics **13**, 17930 (2011).

[3] A. P. Thompson, L. P. Swiler, C. R. Trott, S. M. Foiles, and G. J. Tucker, Journal of Computational Physics **285**, 316 (2015).

[4] V. L. Deringer and G. Csányi, Physical Review B **95**, 094203 (2017).

[5] S. Chmiela, A. Tkatchenko, H. E. Sauceda, I. Poltavsky, K. T. Schütt, and K.-R. Müller, Science advances **3**, e1603015 (2017).

[6] K. Schütt, P.-J. Kindermans, H. E. S. Felix, S. Chmiela, A. Tkatchenko, and K.-R. Müller, in *Advances in Neural Information Processing Systems* (2017) pp. 991–1001.

[7] V. L. Deringer, C. J. Pickard, and G. Csányi, Physical review letters **120**, 156001 (2018).

[8] A. P. Bartók, J. Kermode, N. Bernstein, and G. Csányi, Physical Review X **8**, 041048 (2018).

[9] L. Zhang, J. Han, H. Wang, R. Car, and E. Weinan, Physical review letters **120**, 143001 (2018).

[10] L. Zhang, J. Han, H. Wang, W. Saidi, R. Car, and E. Weinan, in *Advances in Neural Information Processing Systems* (2018) pp. 4441–4451.

[11] V. Botu, R. Batra, J. Chapman, and R. Ramprasad, The Journal of Physical Chemistry C **121**, 511 (2016).

[12] E. V. Podryabinkin and A. V. Shapeev, Computational Materials Science **140**, 171 (2017).

[13] A. Mishra, S. Hong, P. Rajak, C. Sheng, K.-i. Nomura, R. K. Kalia, A. Nakano, and P. Vashishta, npj Computational Materials **4**, 42 (2018).

[14] J. P. Janet, C. Duan, T. Yang, A. Nandy, and H. Kulik, Chemical Science (2019).

[15] F. Musil, M. J. Willatt, M. A. Langovoy, and M. Ceriotti, Journal of chemical theory and computation **15**, 906 (2019).

[16] L. Zhang, D.-Y. Lin, H. Wang, R. Car, and E. Weinan, Physical Review Materials **3**, 023804 (2019).

[17] E. V. Podryabinkin, E. V. Tikhonov, A. V. Shapeev, and A. R. Oganov, Physical Review B **99**, 064114 (2019).

[18] `https://github.com/mir-group/flare`.

[19] J. Behler, The Journal of chemical physics **134**, 074106 (2011).

[20] A. P. Bartók, R. Kondor, and G. Csányi, Physical Review B **87**, 184115 (2013).

[21] A. P. Bartók, M. C. Payne, R. Kondor, and G. Csányi, Physical review letters **104**, 136403 (2010).

[22] A. P. Bartók and G. Csányi, International Journal of Quantum Chemistry **115**, 1051 (2015).

[23] C. K. Williams and C. E. Rasmussen, *Gaussian processes for machine learning*, Vol. 2 (MIT Press Cambridge, MA, 2006).

[24] Z. Li, J. R. Kermode, and A. De Vita, Physical review letters **114**, 096405 (2015).

[25] F. H. Stillinger and T. A. Weber, Physical review B **31**, 5262 (1985).

[26] M. Rupp, M. R. Bauer, R. Wilcken, A. Lange, M. Reutlinger, F. M. Boeckler, and G. Schneider, PLoS computational biology **10**, e1003400 (2014).

[27] E. Uteva, R. S. Graham, R. D. Wilkinson, and R. J. Wheatley, The Journal of chemical physics **149**, 174114 (2018).

[28] Z. Li, *On-the-fly Machine Learning of Quantum Mechanical Forces and Its Potential Applications for Large Scale Molecular Dynamics*, Ph.D. thesis, King's College London (2014).

[29] A. V. Shapeev, Multiscale Modeling & Simulation **14**, 1153 (2016).

[30] K. Gubaev, E. V. Podryabinkin, G. L. Hart, and A. V. Shapeev, Computational Materials Science **156**, 148 (2019).

[31] K. Gubaev, E. V. Podryabinkin, and A. V. Shapeev, The Journal of chemical physics **148**, 241727 (2018).

[32] R. Jinnouchi, F. Karsai, and G. Kresse, arXiv preprint arXiv:1904.12961 (2019).

[33] R. Jinnouchi, J. Lahnsteiner, F. Karsai, G. Kresse, and M. Bokdam, Physical Review Letters **122**, 225701 (2019).

[34] A. Glielmo, P. Sollich, and A. De Vita, Physical Review B **95**, 214302 (2017).

[35] A. Glielmo, C. Zeni, and A. De Vita, Physical Review B **97**, 184307 (2018).

[36] A. Glielmo, C. Zeni, Á. Fekete, and A. De Vita, arXiv preprint arXiv:1905.07626 (2019).

[37] E. Jones, T. Oliphant, P. Peterson, *et al.*, "SciPy: Open source scientific tools for Python," (2001–), [Online; accessed ¡today¿].

[38] P. Giannozzi, S. Baroni, N. Bonini, M. Calandra, R. Car, C. Cavazzoni, D. Ceresoli, G. L. Chiarotti, M. Cococcioni, I. Dabo, *et al.*, Journal of physics: Condensed matter **21**, 395502 (2009).

[39] S. K. Lam, A. Pitrou, and S. Seibert, in *Proceedings of the Second Workshop on the LLVM Compiler Infrastructure in HPC* (ACM, 2015) p. 7.

[40] H. Sheng, M. Kramer, A. Cadien, T. Fujita, and M. Chen, Physical Review B **83**, 134118 (2011).

[41] A. H. Larsen, J. J. Mortensen, J. Blomqvist, I. E. Castelli, R. Christensen, M. Dułak, J. Friis, M. N. Groves, B. Hammer, C. Hargus, *et al.*, Journal of Physics: Condensed Matter **29**, 273002 (2017).

[42] J. Li, Modelling and Simulation in Materials Science and Engineering **11**, 173 (2003).

[43] A. Dal Corso, Computational Materials Science **95**, 337 (2014).

[44] `https://www.quantum-espresso.org/pseudopotentials`.